

# Stress concentrations, diffusionaly–accommodated grain boundary sliding and the viscoelasticity of polycrystals

L.C. Lee<sup>†</sup>, S.J.S. Morris<sup>†</sup>, J. Wilkening<sup>‡</sup>

<sup>†</sup> Department of Mechanical Engineering, University of California, Berkeley 94720

<sup>‡</sup> Department of Mathematics, University of California, Berkeley 94720

November 13, 2010

## Abstract

Using analytical and numerical methods, we analyze the Raj–Ashby bicrystal model of diffusionaly accommodated grain–boundary sliding for finite interface slopes. In that model, two perfectly elastic layers of finite thickness are separated by a given fixed spatially periodic interface. Dissipation occurs by two processes: time–periodic shearing of the interfacial region; and time–periodic diffusion of matter along the interface. Though two timescales govern these processes, of particular interest is the characteristic time  $t_D$  taken for matter to move by grain–boundary diffusion over distances of order the grain size. Two previously unrecognized features of the loss spectrum in the seismic frequency band  $\omega t_D \gg 1$  are established here. First, we show that if all corners on the interface are geometrically identical, the mechanical loss  $Q^{-1}$  depends on angular frequency  $\omega$  by a strict power law  $Q^{-1} = \text{const.}\omega^\alpha$ . For two sliding surfaces found in a regular array of hexagonal grains, the exponent  $\alpha \sim -0.3$ . Second, our analysis shows that  $\alpha$  decreases slowly as  $\omega$  is increased if corner angle varies along the interface. Ultimately  $Q^{-1}$  is controlled by the corner having the most singular stress behaviour. Though these results are obtained from the idealized bicrystal model, we argue physically that similar behaviour will be found in numerical models of polycrystals.

# 1 Introduction

Motivated by the problem of seismic attenuation, the mechanical loss spectrum of fine-grained mantle minerals has been measured at high temperatures in forced torsional-oscillation experiments (e.g. Gribb & Cooper 1998; Jackson et al. 2004; Sundberg and Cooper 2010). According to these experiments, within the seismic frequency range, the mechanical loss  $\mathcal{L}$  (inverse of the quality factor  $Q$ ) varies with angular frequency  $\omega$  according to a power law:  $\mathcal{L} \propto \omega^{-\alpha}$  with  $0.2 < \alpha < 0.35$ . Gribb & Cooper (1998, §4) summarize the experimental evidence supporting diffusionally-accommodated grain-boundary sliding as the attenuation mechanism in these experiments. To their considerations, we can add the following argument of dynamical similarity (Morris & Jackson 2009a): values of  $\mathcal{L}$  measured as a function of frequency for different grain sizes and temperatures define a single curve when graphed against the dimensionless frequency  $\omega\eta'/\mu$ . Here  $\mu$  is the grain rigidity, and  $\eta'$  is the steady-state viscosity for Coble creep measured in independent uniaxial compression tests. Because  $\eta'$  is controlled by grain-boundary diffusion, it follows that  $\mathcal{L}$  is also. (As discussed by Gribb & Cooper 1998, the experiments are designed to eliminate dislocation damping; grain sizes are kept sufficiently small that, within individual grains, dislocation numbers are negligible for the experimental levels of shear stress.)

Though the experimental results can be fitted by spring-dashpot models containing a sufficient number of elements, Gribb & Cooper (1998) and Cooper (2002) argue that the power-law form of the spectrum can be explained more physically by accounting for the spatial variation of stress within grains. To test that explanation, they use the bicrystal model of grain-boundary sliding described by Raj (1975); two isotropic Hookean layers are separated by a fixed prescribed non-plane interface upon which the shear stress vanishes, and across which the normal velocity is discontinuous owing to (grain boundary) diffusion along the interface. To determine the loss spectrum for that model, Gribb & Cooper (1998) solve the initial-value problem determining the response for a step change in applied stress, and then find the loss spectrum by Laplace transformation. As shown in their Fig.10, the agreement between theory and experiment supports their explanation of the observed power-law spectrum.

That agreement is called into question by recent work. Morris & Jackson (2009b) repeat that calculation using the same assumption of infinitesimal grain boundary topography. The new solution differs from the earlier one in two essentials: the loss spectrum is now obtained directly by imposing a sinusoidally varying boundary stress; and an explicit asymptotic form is obtained giving  $\mathcal{L}$  at high frequencies  $\omega\eta'/\mu \gg 1$ . According to the new solution,  $\mathcal{L}$  decreases much more slowly than Gribb & Cooper predicted; it does not even follow a power law, but instead decays inversely with the logarithm of frequency. Thus, although experimental evidence points to grain-boundary sliding as the explanation for the high-temperature attenuation background, detailed analysis of the simplest (bicrystal) model predicts a spectrum that is qualitatively different from that observed.

Despite that result, we argue here that useful lessons can still be drawn from the bicrystal model, provided the effect of finite interface slopes is included. Using analytical and numerical methods, we show that for the sawtooth or truncated sawtooth interfaces (the mode 1 and mode 2 sliding surfaces of Raj & Ashby 1971), the bicrystal model does indeed predict a power-law spectrum when the slope is finite; for  $\omega\eta'/\mu \gg 1$ , the mechanical loss  $\mathcal{L} \propto (\omega\eta'/\mu)^{-\alpha}$  at high frequencies. Though the exponent  $\alpha$  is uniquely determined by the angle subtended by the corner on these piecewise linear interfaces, the constant of proportionality in the loss relation depends on the orientation of the interface. In the

48 limit of vanishing slope, the new result is consistent with the scaling found by Morris &  
 49 Jackson 2009b.) Further, using a model problem, we argue that, at high frequencies, the  
 50 total dissipation–rate within the sample is determined as the sum of contributions from  
 51 each corner on the interface. The magnitude of individual contributions depends on the  
 52 angle subtended by the corner, and on the stress amplitude at the corner; because the latter  
 53 proves to depend on the orientation of the interface, so too does the dissipation.

54 Though we establish this result for the bicrystal model, we expect a similar result should  
 55 apply in a three–dimensional sample. This result is, of course, a refinement of the Gribb  
 56 & Cooper explanation. It provides a definite picture of where dissipation is occurring; and  
 57 it implies that is fruitless to seek a simple theory making quantitative predictions of  $\mathcal{L}$  for  
 58 a three–dimensional sample. For, although the dissipation is localized, its magnitude and  
 59 scaling with frequency depends on the geometry of grains and corners. Cross–sections of  
 60 experimental samples (e.g. Barnhoorn et al. 2007, fig.1e) do not resemble that of a regular  
 61 hexagonal array, and the 3–dimensional geometry is likely to be even more complex. In  
 62 addition to providing this (negative) guide to model building, our analysis also provides  
 63 quantitative results suitable for testing numerical studies.

64 Following the statement (§2) of the boundary–value problem (b.v.p.) and outline (§3)  
 65 of our numerical method, in §4, we use scaling to show that for a sawtooth interface,  
 66  $\mathcal{L} \propto (\omega\eta'/\mu)^{-\alpha}$  for  $\omega\eta'/\mu \gg 1$ . As Eq.(19) we give the formula relating the power–law  
 67 exponent  $\alpha$  to the angle subtended by the corner on the sawtooth interface. In §5, we  
 68 show that our numerical results agree quantitatively with that power law. Because cross–  
 69 sections of experimental samples show a range of corner angles, some corresponding to  
 70 triple junctions, while others appear to correspond to kinks in the grain boundary, we  
 71 then consider an interface having two different corner angles. According to our numerical  
 72 solutions, the slope of the loss spectrum then decreases gradually with increasing frequency;  
 73 at high frequency, the behaviour of the mechanical loss appears to be controlled by the  
 74 corner having the strongest singular stress behaviour. Consequently, one should not expect  
 75 a single power law to fit the entire range of experimental frequencies. This result might  
 76 account for the range of  $\alpha$ –values found in experimental studies. In §6, we summarize our  
 77 chief results and conclusions.

78 Throughout this work, dimensional variables are denoted by asterisks.

## 79 2 Boundary-value problem

80 Fig. 1 shows the geometry of the bicrystal model. In the model, two perfectly elastic grains  
 81 with rigidity  $\mu$  and Poisson ratio  $\nu$  are separated by an interface  $\mathcal{S}_I$ . The interface is periodic  
 82 with a wavelength  $2\pi/\xi$ , where  $\xi$  is the wavenumber. Because samples in the attenuation  
 83 experiments are subjected to small strains  $O(10^{-6})$  (Jackson *et al.*, 2004), we assume the  
 84 interface position to be time–independent, given by a function  $f^*(x^*)$ . Unit vectors in the  
 85 coordinate directions are denoted by  $\hat{\mathbf{x}}$  and  $\hat{\mathbf{y}}$ ; unit tangent and unit normal vectors of the  
 86 interface are denoted by  $\hat{\mathbf{s}}$  and  $\hat{\mathbf{n}}$ , respectively. Along the upper and lower boundaries at  
 87  $y^* = \pm a/\xi$ , the imposed displacement varies sinusoidally in time with angular frequency  
 88  $\omega^*$  and amplitude  $U_0$ , i.e.  $\mathbf{u}^* = \hat{\mathbf{x}}U_0e^{i\omega^*t^*}$ . The grains are assumed to be undergoing plane  
 89 deformation and the  $x$  and  $y$  components of the displacement vector  $\mathbf{u}^*$  are denoted by  
 90  $u^*(x^*, y^*)$  and  $v^*(x^*, y^*)$ , respectively. Similarly, the Cartesian components of the stress  
 91 and strain tensors are denoted by  $\sigma_{ij}^*(x^*, y^*)$  and  $e_{ij}^*(x^*, y^*)$ , respectively.

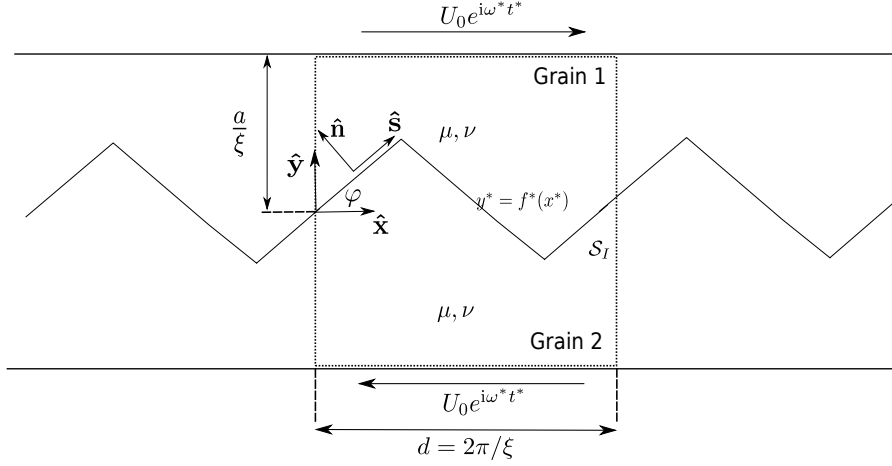


Figure 1: Definition sketch.

92 On the grain interface  $\mathcal{S}_I$ , we impose the following constitutive equations:

$$\ell \sigma_{ns}^* = \eta [\dot{u}_s^*], \quad (1a)$$

93

$$[\dot{u}_n^*] + \frac{v\ell D}{kT} \frac{d^2 \sigma_{nn}^*}{ds^{*2}} = 0. \quad (1b)$$

94

95 The parameters  $\ell$ ,  $\eta$ ,  $v$ ,  $D$ ,  $k$  and  $T$  denote boundary thickness, boundary viscosity, molecu-  
 96 lar volume, grain boundary diffusivity, Boltzmann constant and temperature, respectively.  
 97 Eq. (1a) states that the shear stress along  $\mathcal{S}_I$  is proportional to the discontinuity in the  
 98 tangential velocity across  $\mathcal{S}_I$ . As described by Raj & Ashby (1971), the thin disordered  
 99 boundary phase acts as if it contains a liquid film having uniform viscosity  $\eta$  and constant  
 100 thickness  $\ell$ . We may note that in connection with the steady state creep viscosity  $\eta'$  which is  
 101 the manifestation of diffusion at the grain scale, the boundary viscosity  $\eta$  is a manifestation  
 102 of diffusion at the scale of grain boundaries. Eq. (1b) is obtained by combining Fick's law  
 103 with interfacial mass balance. The volumetric flow rate  $j^*$  (per unit  $z$ -length) along the  
 104 interface due to grain boundary diffusion is related to the normal stress by  $j^* = \frac{v\ell D}{kT} \frac{d\sigma_{nn}^*}{ds^*}$   
 105 in a form analogous to Fick's law (Lifshitz, 1963 and Raj & Ashby, 1971). Using that  
 106 definition of the volumetric flow rate and invoking interfacial mass balance

$$[\dot{u}_n^*] + \frac{dj^*}{ds^*} = 0 \quad (2)$$

107 leads to the second constitutive equation given in (1b). According to (1b), mass flows along  
 108 the interface from regions under compression to regions in tension.

109 Following Mosher & Raj (1974) and Raj (1975), we define the sliding timescale  $t_\eta$  and  
 110 the diffusive timescale  $t_D$  by

$$t_\eta = \frac{\eta}{\xi \ell \mu}, \quad t_D = \frac{kT}{v\ell D \mu \xi^3}. \quad (3a, b)$$

111

112 Physically,  $t_\eta$  and  $t_D$  are, respectively, the timescales on which the two sides of (1a) and  
 113 (1b) balance, if derivatives along the interface scale with its wavelength. We note that

114 if we identify  $2\pi/\xi$  with the grain dimension  $d$ , the timescale  $t_D$  is within a factor of 2  
 115 of the Maxwell time  $\eta'/\mu$  based on the Coble creep viscosity. According to Morris &  
 116 Jackson (2009a, Fig.3) for experiments in the seismic frequency range  $0.1 < \omega_*\eta'/\mu < 10^8$ ,  
 117 and in most cases  $\omega_*\eta'/\mu \gg 1$ . Consequently, though our numerical results will cover  
 118 the whole range of dimensionless frequencies, the limiting behaviour at large dimensionless  
 119 frequencies is of particular interest. At those high frequencies, matter can diffuse along  
 120 the grain boundary only over a distance short compared with the grain size, before the  
 121 time–oscillatory stress reverses. Balancing terms in Eq.(1b), we find that matter diffuses  
 122 over a distance of order the diffusion length defined as follows:

$$\ell_d = \left( \frac{\mu v \ell D}{kT\omega_*} \right)^{1/3}. \quad (4)$$

123 From the identity  $\ell_d\xi = 1/(\omega_*t_D)^{1/3}$ , it follows that for  $\omega_*t_D \gg 1$ ,  $\ell_d \ll d$ , as claimed.

124 Dimensionless variables (without asterisks) are defined as follows:

$$(x^*, y^*) = (x, y)/\xi, \quad (5a)$$

125

$$\mathbf{u}^* = U_0 \mathbf{u}, \quad (5b)$$

126

$$f^* = \varepsilon f/\xi, \quad (5c)$$

127

$$\sigma_{ij}^* = \mu\xi U_0 \sigma_{ij}, \quad (5d)$$

128

$$t^* = t_D t, \quad (5e)$$

129

$$e_{ij}^* = \xi U_0 e_{ij}. \quad (5f)$$

130 In Eq. (5c),  $\varepsilon$  is the characteristic slope of the interface.

131 The dimensionless b.v.p. is as follows:

132

133 in grain 1 and in grain 2 ,

$$\nabla(\nabla \cdot \mathbf{u}) + (1 - 2\nu)\nabla^2 \mathbf{u} = 0; \quad (6a)$$

134 on  $y = \pm a$ ,

$$u = \pm e^{i\omega t}, \quad (6b)$$

135

$$v = 0; \quad (6c)$$

136 on  $y = \varepsilon f(x)$ ,

$$\mathcal{M}[\dot{u}_s] = \sigma_{ns}, \quad (6d)$$

137

$$[\dot{u}_n] + \frac{d^2 \sigma_{nn}}{ds^2} = 0; \quad (6e)$$

138

$$[\sigma_{ns}] = 0 = [\sigma_{nn}] \quad (6f, g)$$

139 on  $x = 2\pi$  and  $x = 0$ ,

$$u(0, y) = u(2\pi, y), \quad (6h)$$

140

$$v(0, y) = v(2\pi, y). \quad (6i)$$

141

142 In (6d), we define the viscosity parameter

$$\mathcal{M} = t_\eta/t_D. \quad (7)$$

143 When  $\mathcal{M} \rightarrow 0$  (fixed frequency), the interface becomes effectively inviscid i.e.  $\sigma_{ns} = 0$ .

144 Problem (6) is linear and time-separable because the interface is fixed. Consequently,  
 145 the solution of (6) for a time-periodic boundary displacement is also time-periodic with  
 146 the same angular frequency  $\omega$ . In the equation of motion (6a), we take the acceleration  
 147 as negligibly small; that approximation is appropriate because the elastic wavelength for  
 148 the experimental frequencies is large compared to the sample size. Because the constitutive  
 149 equations (6d) and (6e) contain time-derivatives, displacements within the sample lag the  
 150 displacements imposed at the boundary. Consequently, the stress at the boundary lags the  
 151 displacement there. The resulting phase lag between the imposed boundary displacement  
 152 and the resultant boundary stress is the expression of dissipation occurring at the interface.

153 By solving (6), we are able to obtain the  $x$ -averaged shear stress  $\tau$  applied at  $y = \pm a$ .  
 154  $\tau$  is defined as

$$\tau(t) = \frac{1}{2\pi} \int_0^{2\pi} \sigma_{xy}(x, a, t) dx. \quad (8)$$

155

156 The sample shear modulus  $G$  is then defined by the equation:

$$G = \tau(t)/\gamma(t), \quad (9)$$

157 where  $\gamma(t) = e^{i\omega t}/a$  is the sample shear strain. Because  $\tau$  and  $\gamma$  are both proportional to  
 158  $e^{i\omega t}$  in (9), the modulus  $G$  is independent of  $t$ .

159 The mechanical loss  $\mathcal{L}$  is defined, as usual, by the equation

$$\mathcal{L} = \tan \arg G. \quad (10)$$

160 If the material can be modelled as a network of springs and dampers, the quantity defined  
 161 in (10) is equal to the ratio of the loss per cycle to  $4\pi$  times the mean strain energy stored  
 162 within the grains (O'Connell & Budiansky, 1978; Bland, 1960).

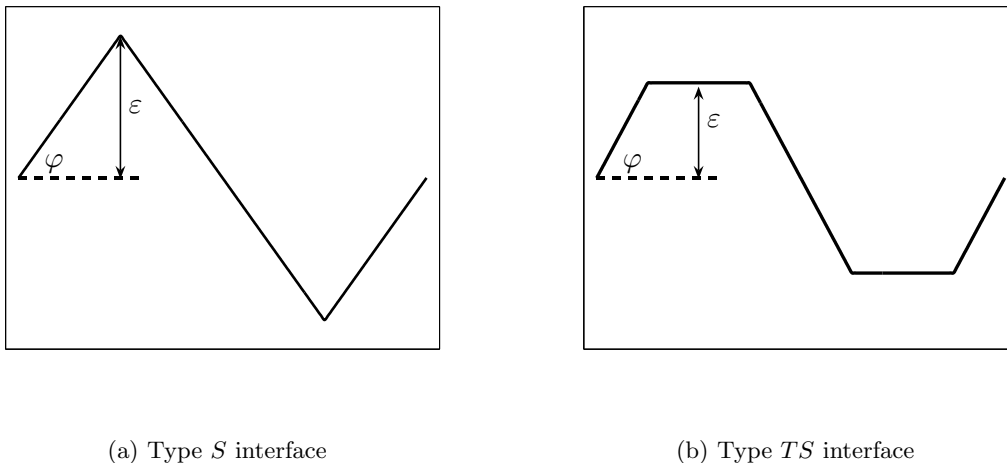


Figure 2: Geometry of interface  $\mathcal{S}_I$

163 We initially consider the two types of interface illustrated in Fig. 2. These interfaces

164 can be represented using piecewise linear functions defined by

$$f = \begin{cases} x/\pi\alpha & \text{if } 0 < x < \pi\alpha; \\ 1 & \text{if } \pi\alpha < x < \pi(1 - \alpha); \\ (\pi - x)/\pi\alpha & \text{if } \pi(1 - \alpha) < x < \pi, \end{cases} \quad (11)$$

165 where the specific values  $\alpha = 1/2$  and  $\alpha = 1/4$  correspond to a type *S* and a type *TS*  
166 interface, respectively. To relate the characteristic slope  $\varepsilon$  to the interface slope angle  $\varphi$ , we  
167 use (13a) and (13b) for the type *S* and the type *TS* interface, respectively.

$$\tan \varphi = \frac{2\varepsilon}{\pi}, \quad \tan \varphi = \frac{4\varepsilon}{\pi}. \quad (13a,b)$$

168

169 These interfaces are found in a regular array of hexagonal grains. In that array, the slope  
170 angles for type *S* and type *TS* interfaces have values  $\varphi = 30^\circ$  and  $\varphi = 60^\circ$ , respectively.

### 171 3 Numerical method

172 Solving b.v.p (6) using conventional finite element method directly is challenging because  
173 boundary condition (6e) requires approximation of the second derivative of normal stress  
174  $d^2\sigma_{nn}/ds^2$ . As a result of the stress concentration described in §4.3, numerical approxima-  
175 tion of the term  $d^2\sigma_{nn}/ds^2$  will incur a large numerical error and requires an excessively  
176 fine mesh near the corners.

177 To avoid computing the second derivative of the normal stress, we use the following  
178 method, based on that of Sethian & Wilkening (2003). Using the principle of superposition,  
179 we decompose problem (6) into two separate b.v.p.s. By doing so, we can recast the original  
180 2-dimensional b.v.p into a 1-dimensional partial differential equation (p.d.e) defined along  
181 the interface  $\mathcal{S}_I$ . That p.d.e is defined by a composite operator embedded with a spatial  
182 differential operator originating from (6e). B.v.p (6) is solved if the eigenvalues and the  
183 eigenfunctions of the composite operator are found. To avoid calculating stress derivatives,  
184 the eigenvalues and the eigenfunctions are found indirectly using a constructed ‘pseudo-  
185 inverse’ of the composite operator. The solution procedure is described in the Appendix  
186 and the details are given in Sethian & Wilkening (2003) and in Lee (2010).

### 187 4 Asymptotes to the loss spectrum

188 To derive the form for these asymptotes, we need the mechanical energy balance. According  
189 to Morris & Jackson (2009b) and Lee & Morris (2010), for the bicrystal system shown in  
190 Fig. 1, the external power supplied at the sample boundaries is either dissipated at the  
191 grain interface  $\mathcal{S}_I$  or stored as strain energy within the perfectly elastic grains, i.e.

$$4\pi\tau \frac{dU}{dt} = \dot{\Upsilon} + \frac{dW}{dt}; \quad (13a)$$

192

$$W = \int_{\mathcal{V}} \left\{ \frac{\nu}{1-2\nu} e_{kk}^2 + e_{ij}^2 \right\} d\mathcal{V}, \quad (13b)$$

193

$$\dot{\Upsilon} = \int_{\mathcal{S}_I} \left\{ \frac{1}{\mathcal{M}} \sigma_{ns}^2 + \left( \frac{d\sigma_{nn}}{ds} \right)^2 \right\} ds \quad (13c)$$

194

195 define the strain energy function  $W(t)$  and the dissipation rate  $\dot{\Upsilon}(t)$ . Here,  $\mathcal{V}$  is the combined  
 196 volume of grain 1 and 2, and  $\tau$  is the  $x$ -averaged shear stress defined in (8). As noted in  
 197 §2, we are taking the grain interface to be time-independent throughout this work.

198

199 Before considering the power-law behaviour that is the main topic of this work, we note  
 200 two results from previous papers. First, according to Morris & Jackson (2009b, Eq.53), for  
 201  $\omega \ll 1$ ,  $\mathcal{L} \propto \omega^{-1}$ . This result can be interpreted as stating that for  $\omega \rightarrow 0$ , the quality factor  
 202  $Q = \mathcal{L}^{-1}$  is proportional to  $\omega$ , as one might expect from Taylor's theorem. Secondly, owing  
 203 to the slip viscosity in Eq.(1a),  $\mathcal{L}$  may have a local maximum describing the loss allowed  
 204 by elastically-accommodated grain-boundary sliding. As discussed by Morris & Jackson  
 205 (2009b), for  $\mathcal{M} \ll 1$ , that local maximum occurs at a large frequency,  $\omega = O(\mathcal{M}^{-1})$ . At  
 206 these very large frequencies, the background loss caused by diffusion becomes negligibly  
 207 small, so that the structure of the resulting loss maximum is as described by Lee & Morris  
 (2010).

208

The power-law spectrum discussed in §1 occurs for  $\mathcal{M} \rightarrow 0$  ( $\omega$  fixed and large). Let  
 209 us consider how the b.v.p. (6) now simplifies. According to Eq.(6d), the shear stress now  
 210 vanishes on the interface:  $\sigma_{ns} = 0$ . The mass balance expressed by Eq.(6e) also simplifies.  
 211 According to Eq.(4), the terms on the left side of Eq.(6e) balance on the dimensionless  
 212 length scale given by  $\ell_d \xi = \omega^{-1/3}$ . Because this scale vanishes with increasing  $\omega$ , at any  
 213 fixed distance from a corner, diffusion along the interface becomes negligibly small, and  
 214 Eq.(6e) simplifies to  $[u_n] = 0$ . According to this discussion, for  $\omega$  fixed and large, and at  
 215 distance  $r$  from the corner that is fixed (possibly small), the interfacial conditions simplify  
 216 to  $[u_n] = 0 = \sigma_{ns}$ . These are the boundary conditions imposed by Picu & Gupta (1996) in  
 217 their local analysis of the stress state near a triple junction. According to their analysis,  
 218 the interfacial normal stress  $\sigma_{nn}$  is given by

$$\sigma_{nn} \propto r^{-\lambda}. \quad (14)$$

219

The stress exponent  $\lambda$  is independent of material properties, and depends only on corner  
 220 angle; it satisfies the condition  $1 > \lambda > 0$ . The first inequality ensures that the strain  
 221 energy is finite, and the second inequality follows because stress is singular at a corner.

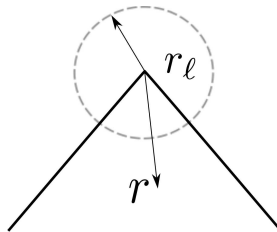


Figure 3: Definition sketch for corner singularity.

222

We use this stress field to estimate the dissipation and strain energy. Because diffusion  
 223 acts to smooth the stress singularity at dimensionless distance  $r_\ell \sim \omega^{-1/3}$ , we estimate  
 224 the corresponding integrals by excluding a small neighbourhood of radius  $r_\ell$  centred on the  
 225 corner. This cut-off length  $r_\ell$  determines the form of the loss spectrum. Using (14) to  
 226 evaluate Eqs (14b), (14c), we find that

$$W \sim \int_{r_\ell}^1 \sigma_{nn}^2 r \, dr \sim 1 - r_\ell^{2(1-\lambda)}, \quad (15a)$$

227

228

$$\Upsilon \sim \frac{1}{\omega} \int_{r_\ell}^1 \left( \frac{d\sigma_{nn}}{dr} \right)^2 dr \sim \frac{1}{\omega} r_\ell^{-(1+2\lambda)}. \quad (15b)$$

229

230 We note that in Eq. (15a), the integration is carried out over an annular region, so that the  
 231 area element scales as  $r dr$ . Because  $\lambda < 1$ , we see that  $W$  approaches a limit as  $r_\ell \rightarrow 0$ ; the  
 232 strain energy  $W$  is not concentrated near the corner. By contrast, the dissipation is focused  
 233 into the corner region, and its magnitude is controlled by the cut-off scale. Substituting  
 234 for  $r_\ell$ , we find that  $\Upsilon \sim \omega^{2(\lambda-1)/3}$ . Using the energetic interpretation of mechanical loss  $\mathcal{L}$   
 235 given below (10), we obtain

$$\mathcal{L} \sim \omega^{-\alpha} \quad (16a)$$

236 where

$$\alpha = \frac{2}{3} (1 - \lambda). \quad (16b)$$

238 Because  $\lambda$  depends on corner angle, so too does  $\alpha$ . Eq. (16) holds for both interfaces  
 239 shown in Fig.2, with one exception. A type  $S$  interface with slope angle  $\varphi = \pm 45^\circ$  coincides  
 240 with the principal axes of stress for simple shear (Lee & Morris 2010). As a result, at  
 241 the high frequencies at which the simplified boundary conditions apply, grains can deform  
 242 under simple shear. The entire stress field is then independent of  $r$ , and the stress exponent  
 243  $\lambda = 0$ . Substituting that value into (16), we find that  $\mathcal{L} \sim \omega^{-2/3}$ . We note that although,  
 244 in this special case, the Picu & Gupta analysis still predicts a non-zero value for the  
 245 stress exponent, the boundary conditions ensure that the amplitude of the corresponding  
 246 eigenfunction is zero. We return to this point in the next section.

247 Fig. 4 summarizes the results given above. If the frequencies defining each region of the  
 248 spectrum are widely separated (i.e.  $1 \ll \omega \ll \mathcal{M}^{-1}$ ), the mechanical loss  $\mathcal{L}$  should scale  
 accordingly as defined in the figure.

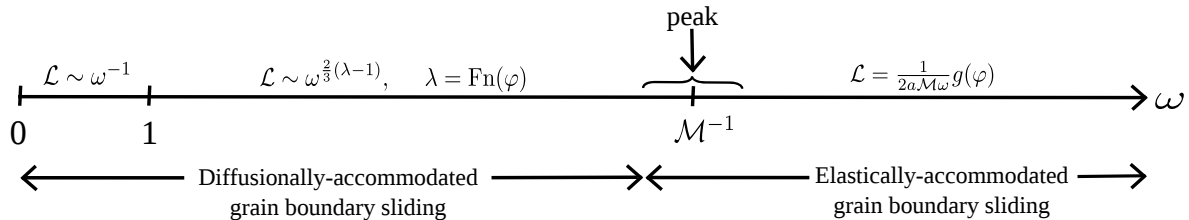


Figure 4: Schematic of the mechanical loss spectrum; for the asymptote for  $\omega\mathcal{M} \gg 1$ , see Lee & Morris (2010).

249

250

251 In addition to predicting the high-frequency asymptote to the loss spectrum for an  
 252 inviscid interface, the scaling argument above also implies that the stress near a corner  
 253 should be self-similar. For within the corner region, both terms in the interfacial mass  
 254 balance (6e) must be of comparable magnitude; moreover, the stress within that inner  
 255 region must match to the outer stress field given by Picu & Gupta. Using Eq.(14), and the  
 256 cut-off scale  $\ell_d$ , we see that values of the interfacial normal stress  $\sigma_{nn}$  computed without  
 257 approximation as a function of distance  $r$  from the corner should define a single curve  
 258 when graphed using the similarity variables  $\sigma_{nn}\omega^{-\lambda/3}$  and  $r\omega^{1/3}$ . This prediction of self-  
 259 similarity allows another test of the arguments underlying the power-law spectrum; it is  
 verified in the next section.

$\varphi$	$\alpha$	$\lambda$	$\lambda_{PG}$
18°	-0.17	0.75	0.79
30°	-0.3	0.55	0.60
45°	-0.66	–	–
58°	-0.49	0.26	0.26

Table 1: Comparing the stress exponent  $\lambda$  derived from the loss spectrum with the value  $\lambda_{PG}$  of Picu & Gupta (1996, Fig.5). See text for explanation.

## 5 Comparison with numerical solutions

We show results for  $0.1 < \omega < 10^8$ , corresponding roughly to the range of dimensionless frequencies encountered in the experiments (e.g. Morris & Jackson 2009a, Fig.3). Results are given for Poisson ratio  $\nu = 0.3$ , comparable to that measured in olivine (Christensen, 1996); our conclusions are insensitive to this choice.

Fig. 5 shows that, as stated in §1, the mechanical loss spectrum is sensitive to the slope angle. For this figure, we have set  $\mathcal{M} = 0$ , so that the interface is inviscid. First, consider, the top curve (slope angle  $\varphi = 0.36^\circ$ ); for  $\omega > 0.2$ , that curve agrees closely with the small-slope, high-frequency asymptote given by Morris & Jackson (2009b, Eq.39). Because that portion of the curve has been obtained by two independent methods, without use of adjustable constants, the agreement provides a test of our numerical method; it also confirms the analysis of Morris & Jackson. The remaining curves ( $\varphi \geq 18^\circ$ ) show that, for the range of  $\omega$  shown,  $\mathcal{L}$  decreases strongly with increasing slope angle; specifically, increasing  $\varphi$  from  $0.36^\circ$  to  $30^\circ$  reduces  $\mathcal{L}$  by about a factor of 10.

To verify the power-law scaling given by (16), we note that for the larger values of  $\varphi \geq 18^\circ$  shown in the figure,  $\mathcal{L}$  varies as  $\omega^{-\alpha}$  for  $\omega \gg 1$ . In Table 1, we give the values of  $\alpha$  obtained by fitting Eq.(19a) to the computed spectrum. The  $\lambda$  shown in column 3 of that table are calculated using (16). Because the normal stress distribution for a type  $S$  interface is exactly an odd function with respect to the corner, these stress exponents  $\lambda$  can be compared to the eigenvalues  $\lambda_{PG}$  associated with an anti-symmetric eigenfunction given by Picu & Gupta (1996, Fig. 5). Comparing columns 3 and 4 of the table, we see that the computed stress exponents  $\lambda$  agree closely with those obtained from the Picu & Gupta analysis, except when  $\varphi = 45^\circ$ . As explained below (16), for that special case,  $\lambda = 0$  and  $\mathcal{L} \sim \omega^{-2/3}$ . That prediction is verified in column 2 of the table. (We do not display the corresponding values of  $\lambda$  and  $\lambda_{PG}$  because, as discussed in §4 above, in this case, they correspond to different eigenfunctions.) The next figure is used to verify the property of self-similarity discussed at the end of §4.

Fig. 6 shows the interfacial normal stress  $\sigma_{nn}$  near a corner as a function of distance  $r$  along the interface, with  $\omega$  as a parameter. The figure verifies the self-similarity of the stress field. We also note that for the type  $S$  interface,  $\sigma_{nn}$  is an odd function of distance along the interface; for this reason,  $\lambda_{PG}$  values cited in table 1 were obtained using the curve given in Fig.5 of Picu & Gupta for an antisymmetric stress field. (We note that the curve labels are interchanged in their figure; the solid line should correspond to the antisymmetric eigenfunction.) The next two figures show the relation between the loss-maximum occurring when  $\mathcal{M} \neq 0$ , and the background spectrum discussed above.

Fig. 7 shows the rigidity  $G$  computed as a function of angular frequency  $\omega$  with  $\mathcal{M}$  as a parameter for a type  $S$  interface with  $\varphi = 30^\circ$ .

Fig. 7a shows  $\mathcal{L}$  as a function of  $\omega$  for a viscous interface. In the curve for  $\mathcal{M} = 10^{-8}$ , all

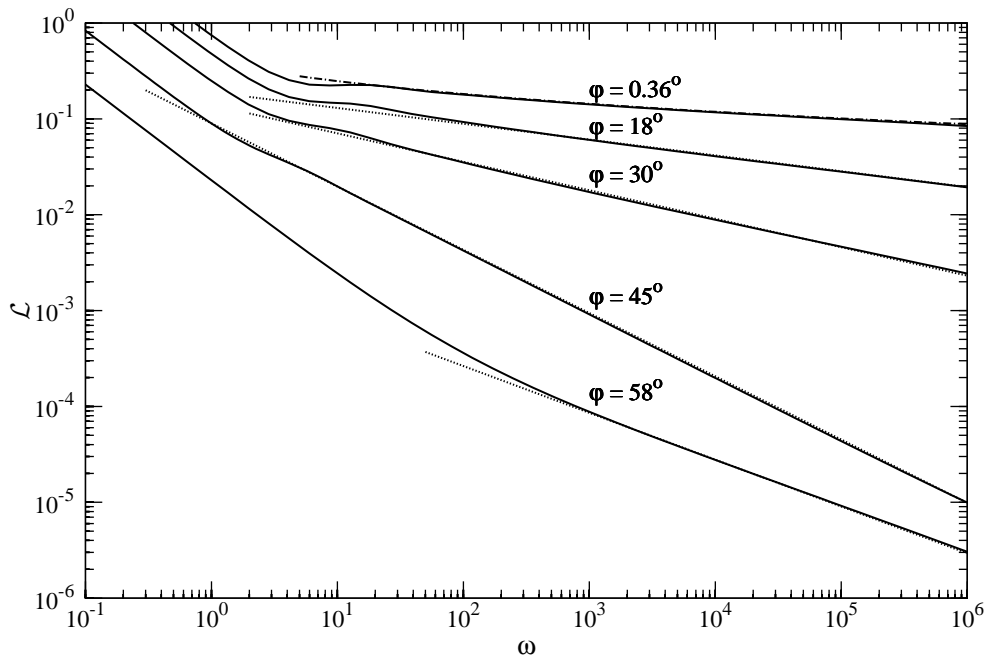


Figure 5: Mechanical loss  $\mathcal{L}$  as a function of angular frequency  $\omega$  when the interface is inviscid  $\mathcal{M} = 0$ . Type  $S$  interface.  $N = 500$ . ..... asymptotes Eq. (16) with  $\lambda$  given in Table 1. - - - - - Morris & Jackson (2009b, Eq. 39b). For other parameters, see caption to Fig. 7.

298 the features summarized in Fig.4 are present: for  $\omega \ll 1$ , the mechanical loss  $\mathcal{L}$  varies as  $\omega^{-1}$ ;  
 299 for  $1 \ll \omega \ll 10^5$ , follows the power-law asymptote discussed above; the local maximum  
 300 due to elastically-accommodated grain-boundary sliding is found at  $\omega \sim 10^{-8}$ ; thereafter,  
 301  $\mathcal{L}$  varies as  $\omega^{-1}$ , as shown in Fig.4. At the local maximum  $\mathcal{L} \simeq 0.05$ , approximately  
 302 equal to the value found in Lee & Morris (2010, Fig.9) for the same values of the control  
 303 parameters. Though we do not show loss spectra for other values of  $\mathcal{M}$  we note that once  
 304 the maximum is clearly visible, its height is independent of  $\mathcal{M}$ ; that is because the loss due  
 305 to diffusionally-accommodated sliding is then small at the peak frequency.

306 The curve for  $\mathcal{M} = 10^{-3}$  is included to show that, when the sliding timescale and  
 307 the diffusion timescale are not widely separated, the loss decreases rapidly with increasing  
 308 frequency, except for a short plateau covering a couple of decades in frequency.

309 Fig. 7b shows the sample rigidity  $|G|$ . From the curve for  $\mathcal{M} = 10^{-8}$ , we see that  
 310 the response consists of two regions of constant  $|G|$  separated by transition regions. The  
 311 first plateau covers the range  $10^2 < \omega < 10^7$ . Within this frequency range,  $\mathcal{L}$  follows the  
 312 power-law asymptote, the shear stress vanishes over most of the interface; because only  
 313 normal stresses act on the interface,  $|G|$  is less than the unit rigidity of the grains. The  
 314 second plateau occurs for  $\omega > 10^8$ . At these high frequencies, the grains behave as if they  
 315 are welded at the interface i.e.  $[u_n] = 0$  and  $[u_s] = 0$ , and  $|G| \rightarrow 1$ . Similar behaviour is  
 316 predicted by the small-slope analysis (Morris & Jackson 2009b).

317 Fig. 8 shows the corresponding results for the type  $TS$  interface. They are included  
 318 to show that the slowly-varying region in the mechanical loss spectrum depends on corner  
 319 orientation, as well as on the angle subtended by the corner. For this type  $TS$  interface  
 320 with  $\varphi = 60^\circ$ , the subtended angle is identical with that of the type  $S$  interface discussed

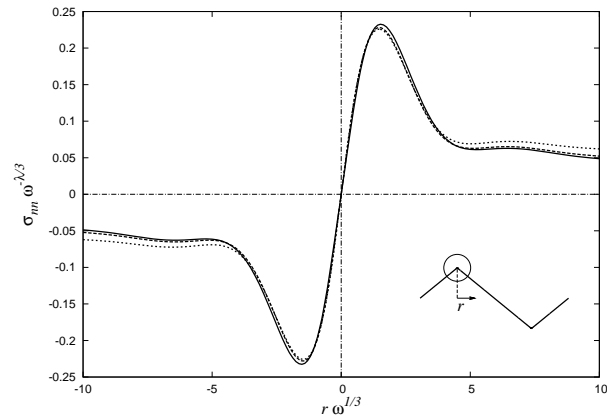
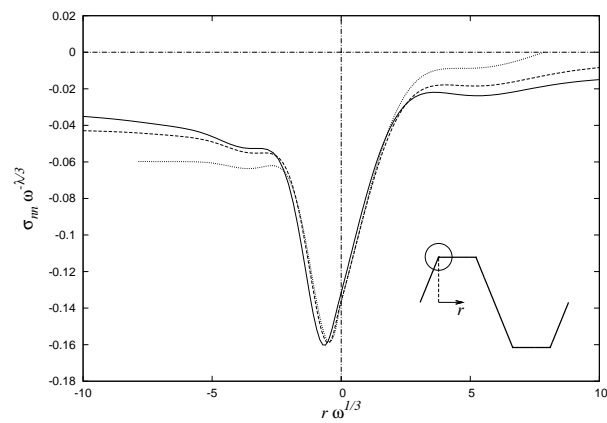
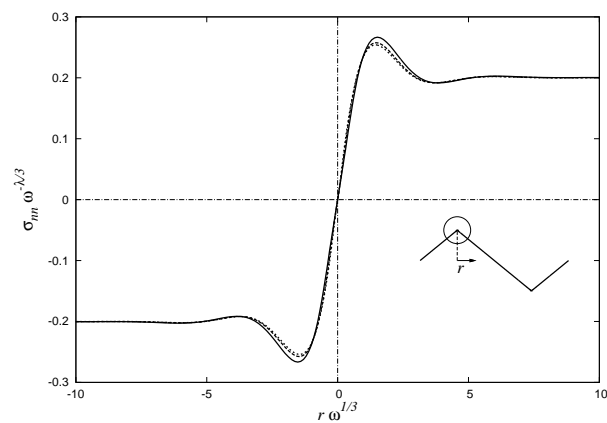
(a) Type *S* interface ( $\varphi = 30^\circ$ )(b) Type *TS* interface ( $\varphi = 60^\circ$ )(c) Type *S* interface ( $\varphi = 45^\circ$ )

Figure 6: Normal stress  $\sigma_{nn}$  distribution near corner. Inset shows geometry. —  $\omega = 10^5$ . - - -  $\omega = 10^4$ . .....  $\omega = 10^3$ . (a) Type *S* interface.  $\varphi = 30^\circ$ .  $\lambda = 0.55$ . (b) Type *TS* interface.  $\varphi = 60^\circ$ .  $\lambda = 0.45$ . (c) Type *S* interface.  $\varphi = 45^\circ$ .  $\lambda = 0$ . Refer to Fig. 7 for other parameters.

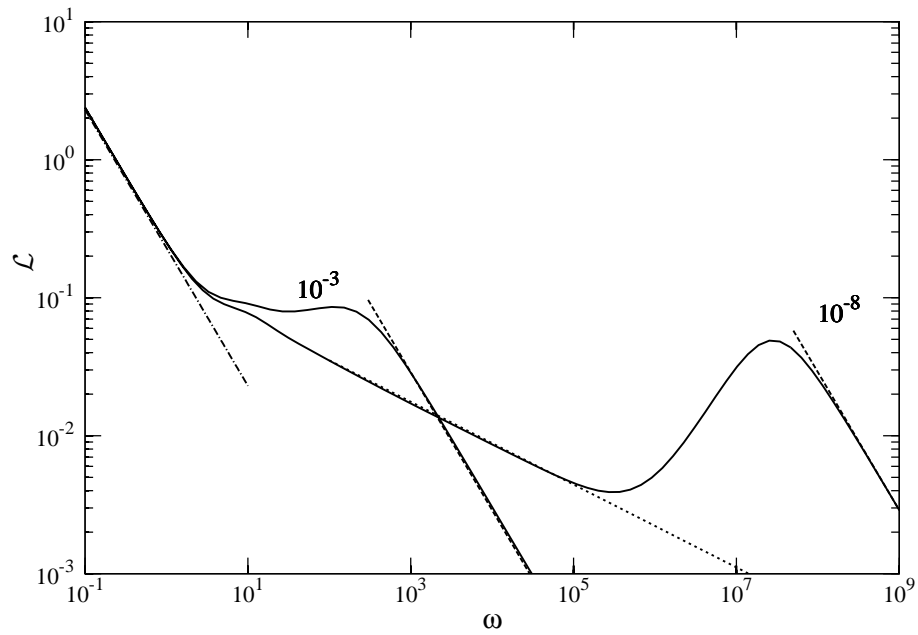
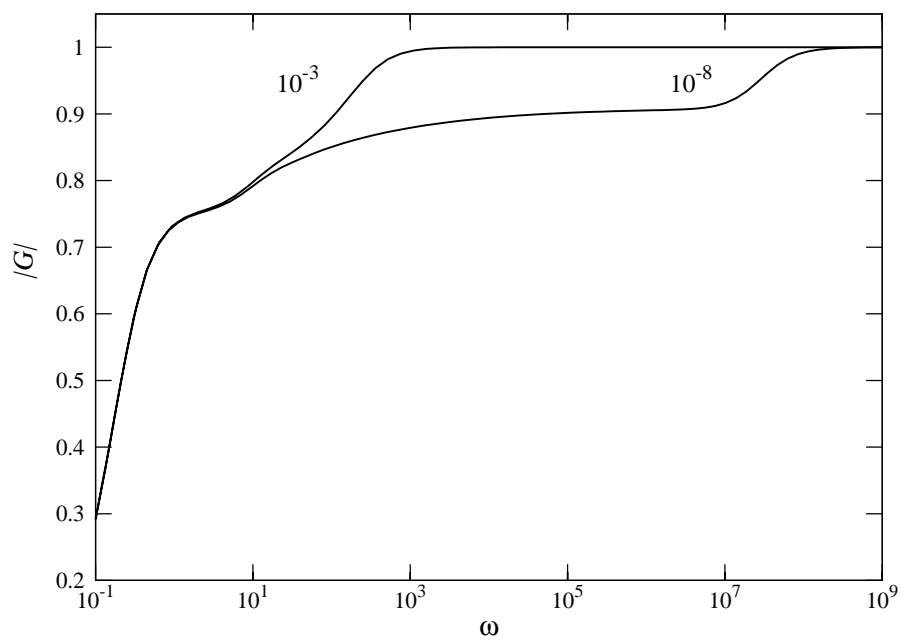
(a)  $\mathcal{L}$ (b)  $|G|$ 

Figure 7: Rigidity as a function of  $\omega$  with  $\mathcal{M}$  as a parameter. Type  $S$  interface,  $a = 5$ ,  $\varphi = 30^\circ$ ,  $\nu = 0.3$ . (a)  $\mathcal{L} = \tan \arg G$ ; (b)  $|G|$ . Curve labels give values of  $\mathcal{M}$ . ----- asymptote  $\mathcal{L} \sim \omega^{-1}$ . ..... asymptote Eq. (16). -.-.-.- asymptote  $\mathcal{L} \sim \omega^{-1}$ . Constant of proportionality is fitted for Eqs (15), (19).

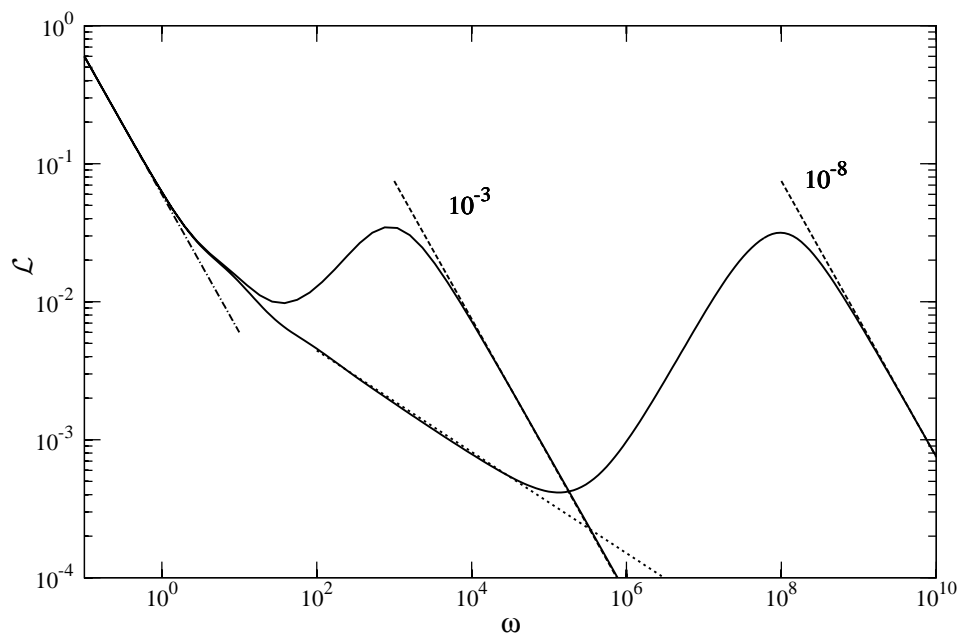
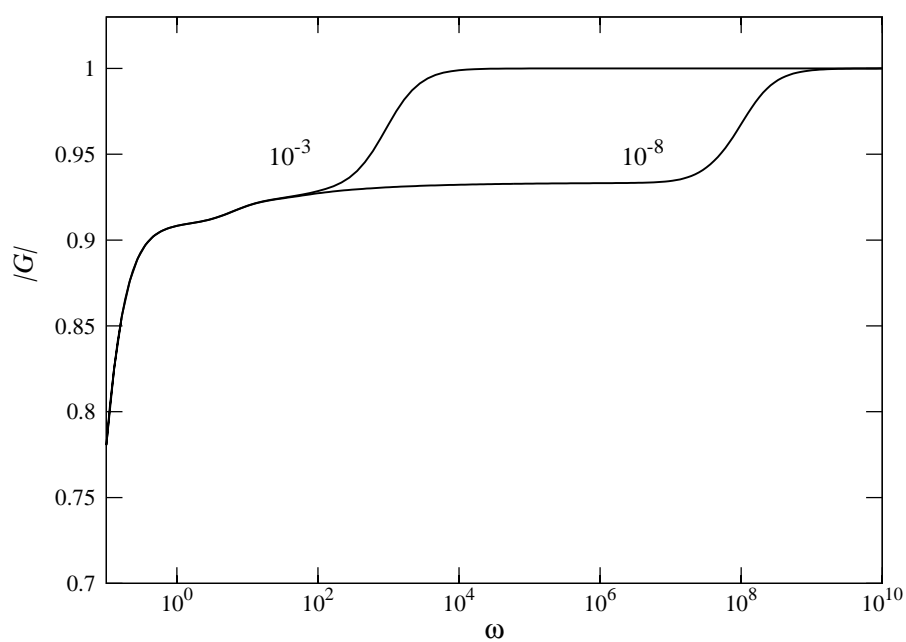
(a)  $\mathcal{L}$ (b)  $|G|$ 

Figure 8: Rigidity as a function of  $\omega$  with  $\mathcal{M}$  as a parameter. Type  $TS$  interface,  $\varphi = 60^\circ$ . (a)  $\mathcal{L} = \tan \arg G$ ; (b)  $|G|$ . See caption to Fig.5 for curve types.

321 in the previous figure. The orientation is different, however. The present figure shows that  
 322 in the power-law régime,  $\mathcal{L}$  decreases more rapidly in the present case. This more rapid

323 decay reflects the parity of the most singular allowable stress eigenfunction. According to  
 324 Fig. 6(a), for the type  $S$  interface,  $\sigma_{nn}$  is an *odd* function of distance along the interface,  
 325 whereas for a type  $TS$  interface,  $\sigma_{nn}$  is nearly an *even* function. Using Picu & Gupta (1996,  
 326 Fig. 5), we find that for a symmetric stress eigenfunction  $\sigma_{nn}$ , the stress exponent  $\lambda = 0.45$ .  
 327 The same value is obtained by fitting the values of  $\mathcal{L}$  shown in Fig. 8 to (16). We conclude  
 328 that although, at high frequencies, dissipation is concentrated near grain corners, we can  
 329 not predict the loss spectrum without accounting for the orientation of grain boundaries.

330 In cross-sections of experimental samples, corner angles of differing sizes. According to  
 331 the results above, each such corner will contribute a characteristic value of  $\alpha$ . The next  
 332 figure shows how two corners having different angles affect the loss spectrum.

333 In cross-sections of experimental samples, corner angles of differing sizes occur. It is  
 334 interesting to see how two corners subtending different angles affect the loss spectrum.  
 335 Because the strain energy  $W$  is insensitive to local stress behaviour, the mechanical loss  $\mathcal{L}$   
 336 can be found by summing the contribution of the dissipation  $\Upsilon$  from each region surrounding  
 337 a corner. Consequently, the mechanical loss  $\mathcal{L}$  behaviour in the slowly-varying region is a  
 338 summation of the power-law scaling associated with each corner. The constants of each  
 339 scaling are determined by the respective constants of proportionality found in the Picu  
 340 & Gupta local stress description. Our scaling analysis suggests that the mechanical loss  
 341 behaviour in polycrystals at sufficiently high frequencies i.e.  $\omega \rightarrow \infty$  will be controlled by  
 342 the corner having the largest stress exponent  $\lambda$ .

343 To test this prediction, we consider an interface illustrated in the inset of Fig. 9 by  
 344 the solid line. Along the interface, there are two different corners  $C_1$  and  $C_2$  having angles  
 345  $\phi_1 = 175^\circ$  and  $\phi_2 = 107^\circ$ , respectively. For these two corners  $C_1$  and  $C_2$ , the local analysis by  
 346 Picu & Gupta (1996) predicts the strongest stress exponents  $\lambda$  to be 1 and 0.5, respectively.  
 347 The behaviour of the mechanical loss  $\mathcal{L}$  at sufficiently high frequencies is therefore expected  
 348 to be controlled by  $C_1$ .

349 Fig. 9 shows the mechanical loss spectrum obtained for the interface shown in the  
 350 inset. There are two main features in the figure. First, the behaviour of the mechanical  
 351 loss is consistent with the above prediction and appears to approach the logarithmic scaling  
 352 i.e.  $1/\ln\omega$  corresponding to a stress exponent  $\lambda = 1$  at  $C_1$ . The graph is truncated at  
 353  $\omega = 5 \times 10^8$  due to a lack of numerical resolution at higher frequencies. Second, the slope  
 354 decreases gradually with frequency in the slowly-varying region due to the diminishing  
 355 effect on the loss spectrum from the other corner  $C_2$ . To show that the effect of  $C_2$  indeed  
 356 diminishes with increasing frequency  $\omega$ , we also graph the scaling  $\mathcal{L} \sim \omega^{-0.33}$  produced by  
 357  $C_2$ .

358 This result is also consistent with the behaviour of the mechanical loss  $\mathcal{L}$  found in  
 359 experiments. Because corner angles in triple junctions vary spatially within polycrystals,  
 360 a gradual decrease in the slope of the mechanical loss spectrum caused by the diminishing  
 361 effect from corners having smaller stress exponents  $\lambda$  is also expected to be observed in  
 362 experiments. This may explain the behaviour seen in Fig.3 of Morris & Jackson (2009), in  
 363 which the measured quality factor  $Q = \mathcal{L}^{-1}$  becomes decreasingly sensitive to  $\omega$  at higher  
 364 frequencies.

## 365 6 Conclusion

366 We have made an analytical and numerical study of diffusionally-accommodated grain  
 367 boundary sliding along a prescribed spatially-periodic finite-slope interface using a bicrystal

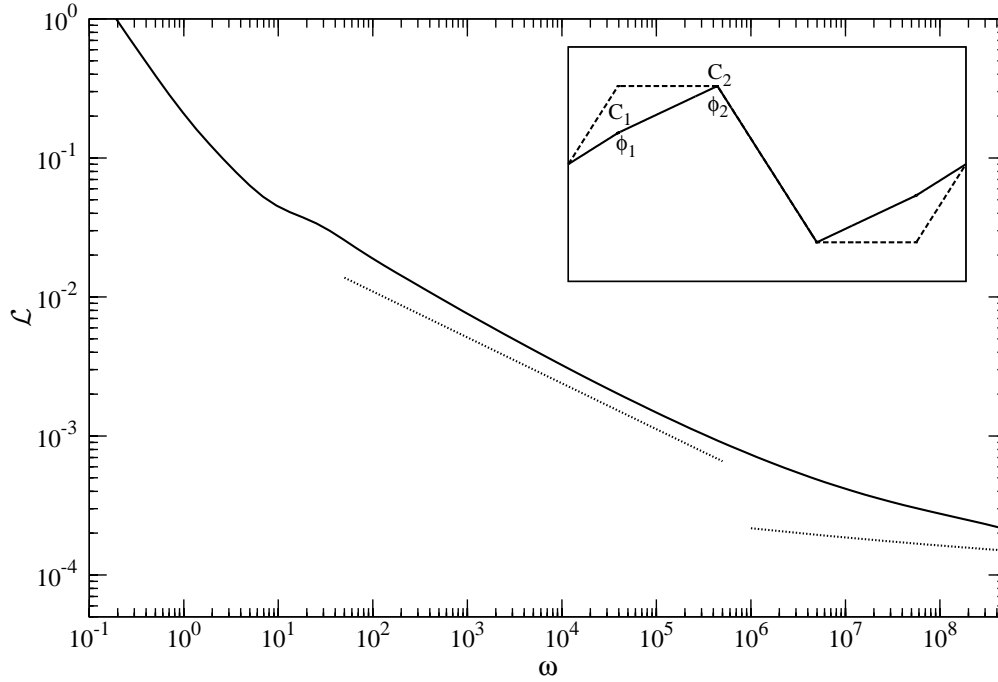


Figure 9: Mechanical loss  $\mathcal{L}$  as a function of angular frequency  $\omega$  for the geometry given in the inset.  $\phi_1 = 175^\circ$ ,  $\phi_2 = 107^\circ$ . Dotted lines:  $\mathcal{L} \sim \omega^{-0.33}$  and  $\mathcal{L} \sim 1/\ln\omega$ . Refer to text for explanation.

368 model. Using scaling analysis, we have derived asymptotes to the mechanical loss spectrum  
 369 and show that our numerical results agree with these asymptotes. Our results show that the  
 370 general features predicted by the small-slope analysis in the mechanical loss spectrum are  
 371 present even for a finite slope interface. Here, we summarize key features in the spectrum  
 372 for a finite-slope interface when the timescales are widely separated i.e. when  $\mathcal{M} \ll 1$ :

- 373 (i) A local maximum is found near frequency  $\omega \sim \mathcal{M}^{-1}$ . That peak stands out from the  
 374 absorption (or high-temperature) background caused by diffusion.
- 375 (ii) For periodic interfaces having sharp corners subtending identical angles, a slowly-  
 376 varying region of the mechanical loss  $\mathcal{L}$  is found at frequencies  $1 \ll \omega \ll \mathcal{M}^{-1}$ .  
 377 Within that region,  $\mathcal{L}$  follows a power-law relation i.e.  $\mathcal{L} \sim \omega^\alpha$ , where  $\alpha$  depends on  
 378 the stress exponent  $\lambda$  by (16). Because of the constraints to the stress exponent  $\lambda$ ,  
 379 the power-law exponent is bounded by  $-2/3 \leq \alpha < 0$ . The parameter  $\alpha$  depends on  
 380 orientation of the sliding surfaces, in addition to the angle subtended by the corner  
 381 (compare Figs 7a,8a).

382 Our analysis suggests that the mild variation of the mechanical loss with frequency that  
 383 is often seen in experiments is likely to be caused by corner stress concentrations. For the  
 384 type  $S$  and the type  $TS$  interfaces found in a regular array of hexagonal grains, the power  
 385 law exponents  $\alpha$  are found to have values -0.3 and -0.37, respectively. These values are  
 386 close to those observed in the experiments. Because these values are also comparable to one  
 387 another, we speculate that the power law exponent controlling the mechanical loss scaling  
 388 in a regular array of hexagonal grains is also  $\sim 0.3$ . That result still needs to be verified  
 389 numerically.

390 In an array of regular hexagons, corner angle is constant along a sliding surface. That is  
391 not so in polycrystals which typically have a range of grain sizes and corner angles. Based  
392 on the preceding analysis, we therefore expect the slope in the loss spectrum to decrease  
393 with increasing frequency as the effects from the corners having weaker stress concentration  
394 diminishes. That result is consistent with the experiments and suggests that the differing  
395 values of power-law exponent  $\alpha$  found experimentally may reflect the differing ranges of  $\omega t_D$   
396 accessed in those experiments. In the high frequency extreme  $\omega \rightarrow \infty$ , the mechanical loss  
397 scaling is predicted to be controlled by the corner having the largest stress exponent. Our  
398 result supports that prediction but due to the limitation of our computational resources,  
399 we are unable to verify it. The result could be verified by using a finer mesh near corners  
400 or by using singularity basis function in the finite element method.

401 We have shown that the behaviour of the mechanical loss spectrum found in the at-  
402 tenuation experiments can be explained using the simplest physical model of diffusionally-  
403 accommodated grain boundary sliding. Because our results show that the loss spectrum is  
404 controlled by local stress behaviour near triple junctions, our prediction should, in princi-  
405 ple, persist even in polycrystals. Our results can therefore be used as a check for numerical  
406 models of polycrystals. To predict a general mechanical loss scaling found in polycrys-  
407 tals, several complications not found in this simple bicrystal model need to be addressed.  
408 These complications are, namely, (i) concurrent sliding along multiple planes, (ii) random  
409 distribution of crystal orientation and corner angles at triple junctions. To address these  
410 complications, one may then have to resort to homogenization techniques.

## 411 Acknowledgement

412 We are grateful to Professor Ian Jackson and Professor Tarek Zohdi for their helpful com-  
413 ments and discussions. We also thank the reviewers for their valuable comments which have  
414 helped us to improve the presentation. L. C. Lee was supported in part by a Committee  
415 on Research Faculty Research Grant to S.J.S Morris from the University of California. Jon  
416 Wilkening was supported by the National Science Foundation through grant DMS-0955078  
417 and by the Director, Office of Science, Computational and Technology Research, US De-  
418 partment of Energy under Contract DE-AC02-05CH11231.

## 419 References

- 420 Barnhoorn, A., Jackson, I., Fitz Gerald, J.D. & Aizawa Y. 2007 Suppression of elastically-  
421 accommodated grain-boundary sliding in high-purity MgO. *J. Eur. Ceram. Soc.* **27**  
422 4697–4703.
- 423 Bland, D. R. 1960 *The theory of linear viscoelasticity*. Oxford: Pergamon.
- 424 Christensen N.I. 1996 Poisson's ratio and crustal seismology *J. Geophys. Res.*, **101**, 3139–  
425 3156.
- 426 Coble, R. L. 1963 A model for boundary diffusion controlled creep in polycrystalline mate-  
427 rials. *J. Appl. Phys.* **34**, 1679–1682
- 428
- 429 Coble, R. L. 1963 A model for boundary diffusion controlled creep in polycrystalline mate-  
430 rials. *J. Appl. Phys.* **34**, 1679–1682
- 431
- 432 Cooper, R. F. 2002 Seismic wave attenuation: Energy dissipation in viscoelastic crystalline

- 433 solids. In *Plastic Deformation of Minerals and Rocks, Rev. Mineral. Geochem.* (ed. S.-i.  
434 Karato & H.-R Wenk) **51**, 253–290
- 435
- 436 Faul, U.H. & Jackson, I. 2007 Diffusion creep of dry, melt-free olivine. *J. Geophys. Res.*  
437 **112**, B04204. (DOI:10.1029/2006JB004586)
- 438
- 439 Faul, U.H., Fitz Gerald, J.D. & Jackson, I. 2004 Shear wave attenuation and dispersion  
440 in melt-bearing olivine polycrystals: 2. Microstructural interpretation and seismological  
441 implications. *J. Geophys. Res.* **109**, B06202. (DOI:10.1029/2003JB002407.)
- 442
- 443 Frost, H.J. & Ashby, M.F. 1982. *Deformation–Mechanism maps*. Pergamon Press.
- 444
- 445 Gribb, T.T. & Cooper, R.F. 1998. Low-frequency shear attenuation in polycrystalline  
446 olivine: Grain boundary diffusion and the physical significance of the Andrade model for  
447 viscoelastic rheology. *J. Geophys. Res.* **103**, 27267–27279.
- 448
- 449 Jackson, I., Faul, U.H., Fitz Gerald, J.D. & Tan, B.H. 2004 Shear wave attenuation and  
450 dispersion in melt-bearing olivine polycrystals: 1. Specimens fabrication and mechanical  
451 testing. *J. Geophys. Res.* **109**, B06201. (DOI:10.1029/2003JB002406.)
- 452
- 453 Lee L.C. 2010 Diffusionally-assisted grain boundary sliding. *Ph.D thesis*. University of  
454 California, Berkeley.
- 455
- 456 Lee L.C. & Morris S.J.S. 2010 Anelasticity and grain boundary sliding. *Proc. R. Soc.*  
457 *A* **466**, 2651–2671.
- 458
- 459 Lifshitz, I.M. 1963 On the theory of diffusion-viscous flow of polycrystalline solids. *Sov.*  
460 *Phys. JETP*, **17**, 909–920.
- 461
- 462
- 463 Morris, S.J.S. & Jackson, I. 2009a Implications of the similarity principle relating creep  
464 and attenuation in finely grained solids. *Mat. Sci. Eng. A*, **521–522**, 124–127.
- 465
- 466 Morris, S.J.S. & Jackson, I. 2009b Diffusionally-assisted grain-boundary sliding and vis-  
467 coelasticity of polycrystals. *J. Mech. Phys. Solids*, **57**, 744–761. (DOI:10.1016/j.jmps.2008.12.006)
- 468
- 469 Mosher, D.R. & Raj, R. 1974 Use of the internal friction technique to measure rates of  
470 grain boundary sliding. *Acta Metall.*, **22**, 1469–1474.
- 471
- 472 O’Connell, R.J. & Budiansky, B. 1978 Measures of dissipation in viscoelastic media. *Geo-*  
473 *phys. Res. Lett.*, **5**, 5–8.
- 474
- 475 Picu, C.R. & Gupta, V. 1996 Stress singularities at triple junctions with freely sliding  
476 grains. *Int. J. Solids Struct.*, **33**, 1535–1541.
- 477
- 478 Raj, R. 1975 Transient behaviour of diffusion-induced creep and creep rupture. *Metall.*  
479 *Trans.*, **2**, 1499–1509.
- 480

481 Raj, R. & Ashby, M. F. 1971 On grain boundary sliding and diffusional creep. *Metall.*  
482 *Trans.*, **2**, 1113–1127.

483

484 Sethian J.A. & Wilkening J. 2003 A numerical model of stress driven grain boundary dif-  
485 fusion. *J. Comput. Phys.*, **193**, 275–305.

486

487 Sundberg M. & Cooper R.F. 2010 A composite viscoelastic model for incorporating grain  
488 boundary sliding and transient diffusion creep; correlating creep and attenuation response  
489 for materials with a fine grain size. *Philos. Mag.*, **90**, 2817–2840.

## 490 Appendix: Solution procedure

491 Because interface  $\mathcal{S}_I$  is time-independent and the b.v.p. given in (6) is linear, the principle  
492 of superposition applies. We decompose that b.v.p into two separate b.v.p.'s which we  
493 denote here as b.v.p<sup>(1)</sup> and b.v.p<sup>(2)</sup>. These two b.v.p.'s share the same geometry shown in  
494 Fig. 1. Using superscripts 1 and 2 to denote, respectively, variables associated with b.v.p<sup>(1)</sup>  
495 and b.v.p<sup>(2)</sup>, the stress field  $\sigma_{ij}$ , strain field  $e_{ij}$  and the displacement fields  $u, v$  of (6) can  
496 be obtained by superposing the solution of the two b.v.p.'s, i.e.

$$\sigma_{ij} = \sigma_{ij}^{(1)} + \sigma_{ij}^{(2)}, \quad (\text{A-1a})$$

$$e_{ij} = e_{ij}^{(1)} + e_{ij}^{(2)}, \quad (\text{A-1b})$$

$$(u, v) = (u^{(1)}, v^{(1)}) + (u^{(2)}, v^{(2)}). \quad (\text{A-1c})$$

497

498 To simplify the notation, we use  $g_n$  and  $g_s$  here to denote, respectively, the normal dis-  
499 placement jump  $[u_n]$  and the tangential displacement jump  $[u_s]$  across the interface  $\mathcal{S}_I$ .  
500 Interfacial stresses and displacement jumps are also denoted using  $2 \times 1$  vector of functions  
501  $\sigma_n = [\sigma_{nn}, \sigma_{ns}]^T$  and  $g = [g_n, g_s]^T$ , respectively.

502 The plane elastostatic equation in Eq. (6a), the periodic boundary conditions in Eqs.  
503 (6h, i) and the requirement that the normal and tangential stresses across the grain bound-  
504 ary are continuous in Eqs. (6f, g) all apply in b.v.p<sup>(1)</sup> and b.v.p<sup>(2)</sup>. The other boundary  
505 conditions are now stated. In b.v.p<sup>(1)</sup>, the boundary conditions at  $y = \pm a$  are

$$u^{(1)} = \pm e^{i\omega t}, \quad v^{(1)} = 0, \quad (\text{A-2a,b})$$

506 and the boundary conditions along the interface  $\mathcal{S}_I$  are

$$\sigma_{ns}^{(1)} = 0, \quad \sigma_{nn}^{(1)} = 0. \quad (\text{A-3a,b})$$

507 Conversely in b.v.p<sup>(2)</sup>, boundary conditions at  $y = \pm a$  are

$$u^{(2)} = 0, \quad v^{(2)} = 0, \quad (\text{A-4a,b})$$

508 whereas boundary conditions along the interface  $\mathcal{S}_I$  are

$$\mathcal{M}\dot{g}_s^{(2)} = \sigma_{ns}^{(2)}, \quad \dot{g}_n^{(2)} + \frac{d^2\sigma_{nn}^{(2)}}{ds^2} = 0. \quad (\text{A-5a,b})$$

509

510 By inspection of b.v.p<sup>(1)</sup>, the two grains do not interact with one another through the  
 511 interface  $\mathcal{S}_I$ . Hence, the two grains move rigidly across one another and the displacement  
 512 field  $\mathbf{u}$  of the upper grain and the lower grain are  $ie^{i\omega t}$  and  $-ie^{i\omega t}$ , respectively. These dis-  
 513 placement fields satisfy all equations given in b.v.p<sup>(1)</sup>, and the resulting normal displacement  
 514 jump and tangential displacement jump across the interface  $\mathcal{S}_I$  are, respectively,

$$g_n^{(1)} = 2e^{i\omega t} \hat{\mathbf{x}} \cdot \hat{\mathbf{n}}, \quad g_s^{(1)} = 2e^{i\omega t} \hat{\mathbf{x}} \cdot \hat{\mathbf{s}}. \quad (\text{A-6a,b})$$

515 We also note that in b.v.p<sup>(1)</sup>, the stress field  $\sigma_{ij}^{(1)} = 0$ .

516 To solve b.v.p<sup>(2)</sup>, we use eigenfunction expansion. In essence, we reduce a 2-dimensional  
 517 problem given in b.v.p<sup>(2)</sup> to a 1-dimensional problem defined along interface  $\mathcal{S}_I$ . We define  
 518 a linear operator  $\mathbf{S}$  that maps the given displacement jumps  $g^{(2)}$  onto the interfacial stresses  
 519  $\sigma_n^{(2)}$ . Note that  $\mathbf{S}$  solves for  $\sigma_n^{(2)}$  when  $g^{(2)}$  is prescribed along the interface  $\mathcal{S}_I$ . Because  
 520 stresses in b.v.p<sup>(1)</sup> are zero, the interfacial stresses in b.v.p<sup>(2)</sup> are equivalent to that in the  
 521 original b.v.p. i.e.  $\sigma_n^{(2)} = \sigma_n = (\sigma_{nn}, \sigma_{ns})^T$ . The operator  $\mathbf{S}$  is defined as follows:

$$\mathbf{S} : g^{(2)} \longrightarrow \sigma_n^{(2)}. \quad (\text{A-7})$$

522 We also define the differential operator  $\mathbf{L}$  as

$$\mathbf{L} : \sigma_n \longrightarrow \left( \frac{d^2 \sigma_{nn}}{ds^2}, -\mathcal{M}^{-1} \sigma_{ns} \right)^T. \quad (\text{A-8})$$

523 In Eq. (A-8),  $\mathbf{L}$  operates separately on functions  $\sigma_{ns}$  and  $\sigma_{nn}$ ; multiplying  $\sigma_{ns}$  with  $-\mathcal{M}^{-1}$   
 524 and taking the second derivative of  $\sigma_{nn}$  with respect to  $s$ . Using the definitions given in (A-7)  
 525 and (A-8), and noting that  $\sigma_n = \sigma_n^{(2)}$ , we find, from the constitutive equations (6d) and (6e)  
 526 of the original b.v.p, that  $\mathbf{L}\mathbf{S}g^{(2)} = \dot{g}$ . Applying the principle of superposition  $\dot{g} = \dot{g}^{(1)} + \dot{g}^{(2)}$   
 527 to that equation, the 2-dimensional elasticity problem is absorbed into the operators leaving  
 528 a single equation governing the time-evolution of the interfacial displacement jumps:

$$\dot{g}^{(2)} + \mathbf{L}\mathbf{S}g^{(2)} = -\dot{g}^{(1)}. \quad (\text{A-9})$$

529 The r.h.s term in (A-9) can be calculated using (A-6).

530 Time evolution of the interfacial gap  $g^{(2)}$  defined in (A-9) can be obtained by eigen-  
 531 function expansion if the eigenvalues  $\gamma_k$  and the eigenfunctions  $Z_k(s)$  associated with the  
 532 composite operator  $\mathbf{L}\mathbf{S}$  are known i.e.

$$\mathbf{L}\mathbf{S}Z_k(s) = \gamma_k Z_k(s). \quad (\text{A-10})$$

533 Using  $N_z$  eigenfunctions, the solution to the homogeneous part of (A-9) (i.e. with  $\dot{g}^{(1)} = 0$ )  
 534 is given by a separable form

$$g_h^{(2)}(s, t) = \sum_{k=1}^{N_z} \beta_k e^{-\gamma_k t} Z_k(s), \quad (\text{A-11})$$

535 where the subscript  $h$  refers to the homogenous solution and  $\beta_k$  are coefficients determined  
 536 by the initial condition  $g_0^{(2)}(s)$ . The coefficients  $\beta_k$  can be found by requiring them to satisfy

$$\sum_{k=1}^{N_z} \beta_k Z_k(s) = g_0^{(2)}(s). \quad (\text{A-12})$$

537 Letting  $\Phi_Z$  be a  $1 \times N_z$  vector containing these eigenfunctions,

$$\Phi_Z = [Z_1(s), Z_2(s), \dots, Z_{N_z}(s)] ; \quad (\text{A-13})$$

538 and  $\Phi_Z^*$  be the adjoint operator of  $\Phi_Z$  so that  $\Phi_Z^* g_0^{(2)}$  is a  $N_z \times 1$  vector of scalars defined  
539 as

$$\Phi_Z^* g_0^{(2)} = \int_{S_I} [Z_1 g_0^{(2)}, Z_2 g_0^{(2)}, \dots, Z_{N_z} g_0^{(2)}]^T ds, \quad (\text{A-14})$$

540 the coefficients  $\beta = [\beta_1, \beta_2, \dots, \beta_{N_z}]^T$ , upon solving (A-11) for  $\beta_k$ , can be written as

$$\beta = (\Phi_Z^* \Phi_Z)^{-1} \Phi_Z^* g_0^{(2)}. \quad (\text{A-15})$$

541 Substituting (A-15) into (A-11), the latter equation can be written compactly as

$$g_h^{(2)}(s, t) = E(t) g_0^{(2)}(s), \quad (\text{A-16})$$

542 where  $E(t)$  is defined as the evolution operator, or propagator

$$E(t) = \Phi_Z e^{-\Lambda t} (\Phi_Z^* \Phi_Z)^{-1} \Phi_Z^* \quad (\text{A-17})$$

543 and  $\Lambda$  is a diagonal matrix defined as

$$\Lambda = \text{diag} [\gamma_1, \gamma_2, \dots, \gamma_{N_z}]. \quad (\text{A-18})$$

544 The solution to the inhomogeneous PDE given in (A-9) can then be obtained using Duhamel's  
545 principle

$$g^{(2)}(s, t) = E(t) g_0^{(2)} - \int_0^t E(t - \bar{t}) \dot{g}^{(1)}(s, \bar{t}) d\bar{t}. \quad (\text{A-19})$$

546 Hence, b.v.p<sup>(2)</sup> is solved, if the eigenvalues  $\gamma_k$  and the eigenfunctions  $Z_k$  of LS defined in  
547 (A-10) are found.

548 The steady-state response of  $g^{(2)}$  can be obtained by setting the first r.h.s term in (A-  
549 19) to zero (because it vanishes as  $t \rightarrow \infty$ ), and setting the lower integration limits in the  
550 second r.h.s term from 0 to  $-\infty$  i.e.

$$g_{ss}^{(2)}(s, t) = - \int_{-\infty}^t E(t - \bar{t}) \dot{g}^{(1)}(s, \bar{t}) d\bar{t}. \quad (\text{A-20})$$

551 The subscript  $ss$  is used here to denote steady-state solution. Substituting (A-17) and  
552 (A-6) into (A-20) and then evaluate the resulting integral, the steady-state response of the  
553 displacement jump in b.v.p<sup>(2)</sup> becomes

$$g_{ss}^{(2)}(s, t) = \hat{g}_{ss}^{(2)}(s, \omega) e^{i\omega t}, \quad (\text{A-21a})$$

554 where its frequency-response is given as

$$\hat{g}_{ss}^{(2)}(s, \omega) = -\Phi_Z \mathbf{D} (\Phi_Z^* \Phi_Z)^{-1} \Phi_Z^* g^{(1)}(s, 0), \quad (\text{A-21b})$$

555 and  $\mathbf{D}$  is a  $N_z \times N_z$  diagonal matrix with its  $k$ -th component given by

$$\mathbf{D}_k = \frac{\omega^2 + i\omega\gamma_k}{\omega^2 + \gamma_k^2}. \quad (\text{A-21c})$$

556 Noting that  $\sigma_n = \sigma_n^{(2)}$ , as explained above (A-7), the steady-state response of the interfacial  
 557 stresses  $\sigma_{n,ss}(s, t) = \hat{\sigma}_{n,ss}(s, \omega)e^{i\omega t}$  can be calculated using the operator  $\mathbf{S}$  i.e.

$$\hat{\sigma}_{n,ss}(s, \omega) = \mathbf{S} \hat{g}_{ss}^{(2)}(s, \omega). \quad (\text{A-22})$$

558 Integrating the  $x$ -projection of  $\hat{\sigma}_{n,ss}(s, \omega)$  along the interface  $\mathcal{S}_I$  then leads to the  $x$ -averaged  
 559 shear stress  $\tau$  defined in (8). The mechanical loss  $\mathcal{L}$  can thereafter be calculated using  $\tau$  as  
 560 described in the main text. Thus for any given interface, the mechanical loss spectrum can  
 561 be obtained by computing the eigenvalues  $\gamma_k$  and the eigenfunctions  $Z_k(s)$  of the operator  
 562  $\mathbf{LS}$ . We thus reduce problem (6) into an eigenvalue problem.

563 To avoid computing the second derivative of  $\sigma_{nn}$ , a pseudo-inverse of  $\mathbf{LS}$  is used, instead,  
 564 to find the eigenvalues and eigenfunctions. The pseudo-inverse  $\mathbf{A}$  has the same eigenfunc-  
 565 tions  $Z_k(s)$  as  $\mathbf{LS}$ , and its eigenvalues  $\zeta_k$  are related to those of  $\mathbf{LS}$  by

$$\zeta_k = \begin{cases} \gamma_k^{-1} & \text{if } \gamma_k \neq 0 \\ 0 & \text{if } \gamma_k = 0 \end{cases}. \quad (\text{A-23})$$

566 The pseudo-inverse  $\mathbf{A}$  is constructed using finite element methods; details are given in Lee  
 567 (2010) and Sethian & Wilkening (2003).